Effects of local grain size and inclusions on the low-temperature toughness of low-carbon as-quenched martensite

Sakari Pallaspuro, Saara Mehtonen, Jukka Kömi, Zhiliang Zhang, David Porter

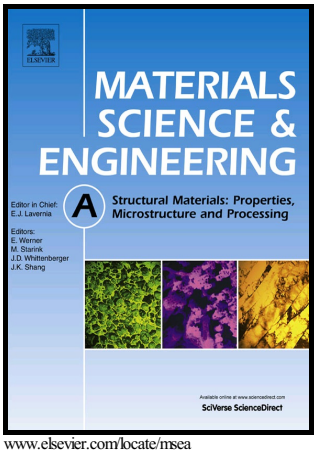

www.elsevier.com/locate/msea

PII: S0921-5093(18)31631-9
DOI: https://doi.org/10.1016/j.msea.2018.11.105
Reference: MSA37225

To appear in: *Materials Science & Engineering A*

Received date: 21 August 2018
Revised date: 20 November 2018
Accepted date: 22 November 2018

Cite this article as: Sakari Pallaspuro, Saara Mehtonen, Jukka Kömi, Zhiliang Zhang and David Porter, Effects of local grain size and inclusions on the low-temperature toughness of low-carbon as-quenched martensite, *Materials Science & Engineering A,* https://doi.org/10.1016/j.msea.2018.11.105

Effects of local grain size and inclusions on the low-temperature toughness of low-carbon as-quenched martensite

Sakari Pallaspuro[a,c,*], Saara Mehtonen[b], Jukka Kömi[a], Zhiliang Zhang[c], David Porter[a]

[a]Materials and Production Engineering, Centre for Advanced Steels Research, University of Oulu, Finland

[b]SSAB, Rautaruukintie 155, PO box 93, 92101 Raahe, Finland

[c]Department of Structural Engineering, Faculty of Engineering Science and Technology, NTNU, Norway

[*]Corresponding author; Materials and Production Engineering, University of Oulu, PL 8000, 90014 Oulun yliopisto, Finland; sakari.pallaspuro@oulu.fi

Abstract

The segregation of alloying elements that occurs during the solidification of steel leads to microscale and macroscale microstructural heterogeneity that can cause anomalous mechanical behaviour. The centreline macrosegregation of a cast and its increased inclusion content are usually considered to be particularly detrimental in the case of conventional structural steels. Samples from centreline and off-centreline positions in a single continuously cast slab of an ultrahigh-strength steel were subjected to hot rolling, reheating and water quenching to 12 mm thick fully martensitic plates to explore the differences in mechanical properties between a homogeneous clean matrix and a heterogeneous inclusion-rich centreline. Despite the presence of strong macrosegregation and a high inclusion content, the centreline material has a significantly better, i.e. a 15 °C lower, fracture toughness reference temperature T_0. However, neither the 28 J Charpy V impact toughness transition temperature T_{28J} nor the tensile properties show notable differences. The inclusion rich heterogeneous material achieves its unexpected toughness properties despite the higher hardness of the centreline and an abundance of large inclusions. Thorough microstructural characterisation shows that the centreline enrichment of alloying elements and impurities leads to a profound refinement in the local grain size, which more than compensates for the expected detrimental effects of the

inclusions and the harder microstructure. The results have practical importance regarding the levels of macrosegregation and inclusion contents that can be tolerated by ultrahigh-strength steels.

Keywords: Fracture toughness; Impact toughness; Ductile-brittle transition temperature; T_0; T_{28J}; Inclusions; Grain size

1. INTRODUCTION

Macrosegregation during the solidification of steels is generally considered to lead to impairment and anisotropy of mechanical properties due to the local enrichment of impurities and elements that increase hardenability and hardness. While localised microsegregation on the size scale of dendrite side-arms can be mitigated by subsequent homogenisation heat treatment, solid state diffusion is too slow to enable the homogenisation of macrosegregation [1]. The differences in local composition persist through the processing of the steel product affecting e.g. in low-alloy steels, austenite recrystallisation kinetics and grain growth, hardenability and phase transformation temperatures, and the formation and growth of carbides. The strongest macrosegregations are associated with the last pools of liquid to solidify making them prone to the highest contents of non-metallic inclusions, which are also generally considered as detrimental to toughness properties.

In the case of continuously cast steel slabs, the central equiaxed area being the last to solidify tends to contain larger non-metallic inclusions, commonly based on e.g. Al, Ca, Mn and Ti, due to the longer time available for them to grow. If there is also centreline macrosegregation, the locally higher content of e.g. Mn and Ti tends to exacerbate the growth of e.g. detrimental MnS, TiN and Ca-based inclusions [2–5]. On the other hand, the higher contents of alloy elements in the centreline segregation can lead to finer

austenite grain sizes via their effect on austenite recrystallisation and grain growth, either via their effect in solid solution or indirectly through the formation of microalloy carbides and nitrides that have a pinning effect on grain boundaries [6]. The central region of continuously cast slabs becomes the centreline of the final steel plate, the properties of which are important for the toughness behavior of the steel structures made from the plate: the plastic constraint and triaxial stresses that arise when the structure is loaded are highest in the central part of the plate, which is the region where brittle failures originate in up to 90% of cases [7].

The critical factors that determine the brittle fracture toughness can be divided into three commonly addressed types: 1) small particles, like carbides and carbide clusters [8–11], 2) larger inclusions and brittle second phase particles [3–5,12–14], and 3) grains [15–18]. These have been used, both interchangeably and often indirectly, to describe toughness properties both at very low temperatures, where toughness is crack nucleation controlled, and at temperatures in the ductile-brittle transition temperature (DBTT) region, where toughness is controlled by crack propagation [15]. More often than not, failure initiation can be a complicated interaction between large grains and large particles [19–21]. Due the ability of grain boundaries to hinder crack propagation and cause local crack arrests, the importance of the effective of grain size is emphasised in the impact toughness test [21], where total absorbed energy is commonly used as the measure of toughness.

Splitting, also known as delamination, can be observed on the fracture surfaces of thermomechanically rolled steels, usually in impact toughness specimens, as cracks formed parallel to the rolling plane and normal to the specimen crack plane. It is often associated with segregation and manifests local anisotropy of toughness [22–25]. The splits introduce an internal size effect to toughness specimens making full-size specimens

behave like a packet of sub-sized specimens by reducing the plane strain constraint, which in turn increases the proportional amount of shear lips. On the upper shelf, this reduces upper shelf energy [26], since crack propagation by ductile tearing absorbs about twice the energy of a fully shear fracture [27].

On the other hand, several studies show that splitting increases the absorbed energy at the ductile-brittle transition temperature region towards the lower shelf and so lowers the resulting transition temperatures [22,24–26,28]. This is due to two dominant factors. The first is the above-mentioned higher fraction of shear lips, the propagation of which consumes more energy than brittle cracks irrespective of the fracture morphology in the splits. Secondly, splitting increases the absorbed impact energy by creating additional fracture surfaces perpendicular to the main fracture plane [22,28]. Even though the impact energy per unit area is slightly smaller for the splits than for the main crack plane, generating splits can toughen the material in the DBTT region [28].

The above factors are important for the development of tough ultrahigh-strength structural steels and the assessment of their weakest links. These steels can possess adequate toughness, weldability and formability, in the as-quenched state even without tempering, when based on low carbon contents and produced by thermomechanically controlled rolling and direct quenching [29]. A common feature of these as-quenched ultrahigh-strength steels is that they do not obey the widely adopted [30–32] correlation of Ref. [33] between the fracture toughness reference temperature T_0 and impact toughness transition temperature T_{28J} [34,35]. To overcome this, Wallin et al. [36] have proposed an updated correlation that estimates the T_0 satisfactorily over a wide range of yield strengths. Pallaspuro et al. [37] have recently highlighted the importance of the coarsest grains for low-temperature toughness based on characterisation of microstructures that were considered internally homogeneous.

In the present study, we distinguish the microstructural features governing the impact toughness and fracture toughness transition temperatures in a heterogeneous system by investigating the influence of locally varying properties. The competition between the weakest link candidates is investigated by characterising a "clean" homogeneous microstructure and a "dirty" inclusion rich segregated heterogeneous microstructure.

2. Materials and methods

2.1. Materials

The material is an experimental continuously cast 210 mm thick slab of a nominally 0.13 wt.% carbon steel selected specifically for this study. A complete cross-sectional slice, 270 mm long in the casting direction, was cut from the slab, and from this slice, central blocks were cut with a width of 80 mm through the whole 210 mm thickness. These blocks were then sawed into three pieces 62.5×80×270 mm (H×W×L), with the cast surfaces removed. In this way, the central piece of the slab with equiaxed grains, a high inclusion content, and centreline segregation, referred to as material "CL" for centre-line, was separated from the cleaner columnar material of the top piece, referred to as material "MM" for matrix material. These pieces were first soaked at 1050 °C for two hours, and then hot-rolled with a Carl Wezel laboratory rolling mill to a 12 mm final thickness with a total reduction of 0.44 below the non-recrystallisation temperature. After the final pass at 850 °C, the plates were directly quenched in water to room temperature with an average cooling rate of 90 °C/s. Temperature was constantly measured with a K-type thermocouple inserted into a hole drilled prior to rolling. The quenched plates were subsequently reaustenitised at 870 °C with a holding time at peak temperature of 20 minutes, and finally water-quenched to room temperature. We produced two similar steel

plates from adjacent pieces of each material using identical process parameters to obtain a representative sample size. We paid special attention to the heat treatments and hot rolling to produce and retain a fine equiaxed prior austenite grain (PAG) structure so that the observed effects of inclusions and segregation on toughness would be relevant to industrially produced steel plates.

2.2. Mechanical testing

Impact toughness and fracture toughness tests were used to evaluate the effects of the microstructural inhomogeneities on the impact toughness transition temperature T_{28J} and the fracture toughness reference temperature T_0, i.e. the temperature at which $K_{Jc(1T)}$ = 100 MPa√m [38], which we later also refer to as the transition temperature. Charpy V-notch (CVN) impact testing according to EN ISO 148-1 [39] was used to determine the 28 J transition temperature T_{28J} and the upper shelf energy (US) using full-sized 10 mm thick specimens tested in the temperature range [-80, +40] °C. Exponential fitting [27] of results was used to determine T_{28J}. Fracture toughness tests were performed according to the standard ASTM E1921 [38] using 10 mm thick single-edge notched bending (SENB) specimens with an a/W ratio of 0.5 in the temperature range [-60, +5] °C. Toughness testing was performed on both longitudinal-transverse (LT) and transverse-longitudinal (TL) specimens [40]. For both types of specimen, the notch is cut in the long side of the specimen in the thickness direction. LT means that the long side of the specimen is parallel to the longitudinal (L, i.e. rolling) direction and the fracture propagates in the transverse (T) direction, and TL means the long side of the specimen is parallel to the transverse direction and the fracture propagates in the L direction. Room-temperature tensile tests were done with an MTS 250 kN test machine in accordance with the standard EN ISO 6892-1 [41] using rectangular 10 mm thick specimens.

2.3. Materials characterisation

We carried out a range of different analyses to study both the global and local microstructural properties. The PAG structure was studied from picric acid etched microsections with a laser scanning confocal microscope, the general microstructure from nital etched samples and the effective grain size (> 15° misorientation between the grains) from samples polished with colloidal silica suspension. A ZEISS Sigma field-emission scanning electron microscope equipped with an EDAX Hikari XP electron backscatter diffraction (EBSD) camera and EDAX TSL OIM software was used for fractography and to study the microstructure, and effective grain size. To clean up the EBSD data captured with a 0.1 µm step size, points with a confidence index lower than 0.1 were excluded, grain confidence index standardisation (tolerance 2.5°, min. size 5 pixels) and 3rd level neighbour orientation correlation were used. We identified the primary cleavage fracture initiation sites from both SENB and CVN specimens by following the river patterns on the fracture surfaces in regions narrowed down with the aid of an optical stereo light microscope.

The bulk chemical compositions were determined with an optical emission spectrometer (SS-OES) and with combustion analysis for the elements H, C, N, O and S. Large-scale through-thickness chemical contents were determined from RD-TD sections with a Spectruma GDA 750 GD-OES using a two-mm spot size and a minimum of three material-consumptive measurements per spot. Local chemical components were mapped with a Jeol JXA-8200 electron probe microanalyser (EPMA) in WDS mode over the thickness-wise central area of the materials, using a 10 µm spot and 20 µm step size excluding obvious inclusion-affected artefacts from the data.

Inclusions were mapped with a Jeol 7000 scanning electron microscope equipped with an XMAX 80 EDS detector and INCA software using a 10 mm working distance, a

15 kV accelerating voltage, a 20 μm aperture and 500 x magnification. After appropriate contrast based thresholding of 46 mm^2 area from longitudinal – plate normal plane per plate, the spectra of all inclusions with an equivalent circle diameter of 0.9 μm or larger were collected from the whole inclusion area. The inclusions were classified into relevant groups using a recognition threshold of 5 wt.% for all the detected elements. Iron, where detected, was removed from the compositional results and all the other element contents were normalised to 100%.

Through-thickness macroscopic hardness was measured, and the hardness of martensite (HV_M) was estimated based on locally varying chemical compositions using Eq. [1] from Blondeau et al. [42], where V_R is the cooling rate. The equation is widely used to estimate hardness of martensite in continuously cooled low-alloy steels [43] and their welds [44]. The possible presence of residual austenite was examined using a Siemens D5000 XRD device. Carbide size was determined with a dedicated plug-in in Photoshop 7.0 from binarised SEM images rejecting data smaller than one nm. All the sizes of microstructural units are given as equivalent circle diameters (ECD).

$$HV_M = 127 + 949C + 27Si + 11Mn + 8Ni + 16Cr + 21log_{10}V_R \qquad [1]$$

3. RESULTS

3.1. Mechanical properties

Table 1 presents the various strength and toughness properties of the two materials. Based on the tensile properties, i.e. yield strength (σ_{YS}), tensile strength (σ_{TS}), and uniform elongation (A_g), the two materials are equal. Impact toughness follows the same line with the transition temperature T_{28J} being insignificantly different at $p \geq 0.10$ (Fig. 1). With the material CL, splitting raises the average absorbed energy for the LT oriented specimens that were tested at -60 °C, and causes an apparent discrepancy for the exponential fitting

(Fig. 1 b). For both materials, T_{28J} is around -50 °C in the LT orientation and around -35 °C in the TL orientation. The upper shelf toughness (US) is better in the material MM in both orientations.

Fig. 2 presents the fracture toughness test results as $K_{Jc(1T)}$ values, thickness-corrected to give the equivalent toughness values of 1-inch thick specimens as per ASTM E1921 [38]. Surprisingly, T_0 of CL is significantly better than MM ($p < 0.0001$), being 13 °C lower in the LT and 16 °C lower in the TL orientation. Here too the material inhomogeneity of CL is visible as more pronounced scatter of the individual data points. In a given temperature, CL specimens with splits have higher fracture toughness than the specimens without them.

Table 1 shows T_0 also as estimated from the exponential-fitted values of the 28 J impact transition temperatures. The conventional formula for estimating T_0 ($T_{0,E1}$ [33]) gives values that are far from the measured values on the unconservative side. However, both MM and CL materials fall inside the estimate of $T_{0,E2}$ [35] that was developed for as-quenched microstructures and of $T_{0,E3}$ [36] that applies to the whole range of ferritic structural steels.

Table 1. Strength and toughness of the study materials.*

Material & orientation		σ_{YS} [MPa]	σ_{TS} [MPa]	A_g [%]	T_{28J} (exp.) [°C]	US [J]	T_0 [°C]	Est. $T_{0,E1}$ [°C] [33]	Est. $T_{0,E2}$ [°C] [35]	Est. $T_{0,E3}$ [°C] [36]
MM	L / LT	963 ± 18	1252 ± 14	3.6 ± 0.2	-49 ± 10 (18)	205	-22 ± 6 (16)	-68	-26	-34
	T / TL	1012 ± 28	1251 ± 15	2.8 ± 0.8	-38 ± 10 (22)	159	-20 ± 6 (16)	-55	-16	-17
CL	L / LT	970 ± 5	1258 ± 3	3.8 ± 0.3	-54 ± 10 (22)	185	-35 ± 6 (17)	-81	-36	-38
	T / TL	993 ± 1	1250 ± 23	3.2 ± 0.5	-33 ± 10 (24)	130	-36 ± 6 (16)	-56	-16	-14

* L = longitudinal, LT = longitudinal-transverse, T = transverse, TL = transverse-longitudinal, σ_{YS} = 0.2% offset proof stress as yield strength, σ_{TS} = tensile strength, A_g = uniform elongation, T_{28J} = Charpy V impact toughness transition temperature, US = Charpy V upper shelf toughness, T_0 = fracture toughness reference temperature. Values marked ± are standard deviations, and values in parentheses are numbers of parallels. Tensile properties are based on two parallels.

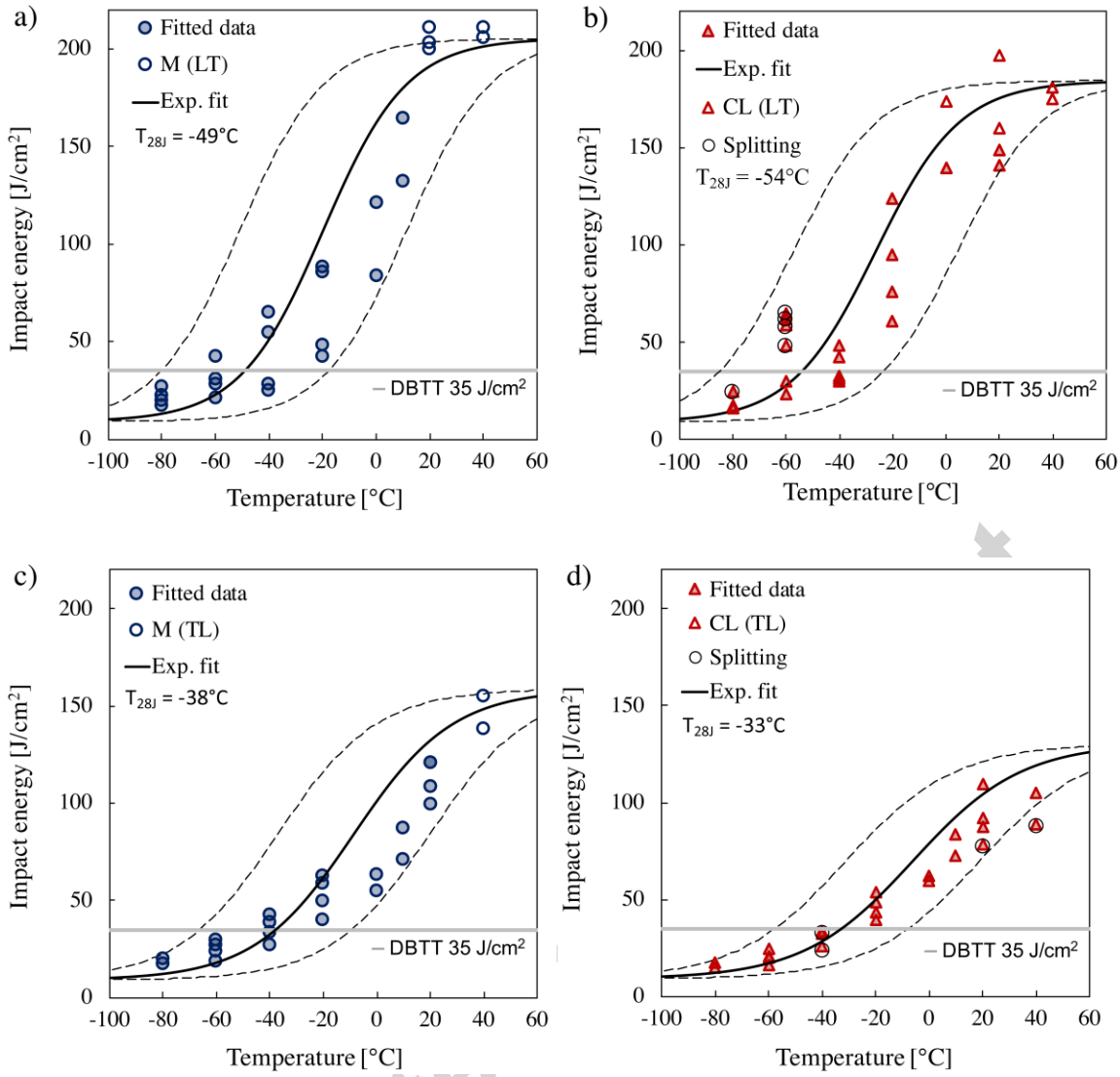

Fig. 1. Impact toughness with fitted ductile-brittle transition curves and their 95% confidence limits of a) MM (LT), b) CL (LT), c) MM (TL) and d) CL (TL). Specimens with splits are marked with black circles.

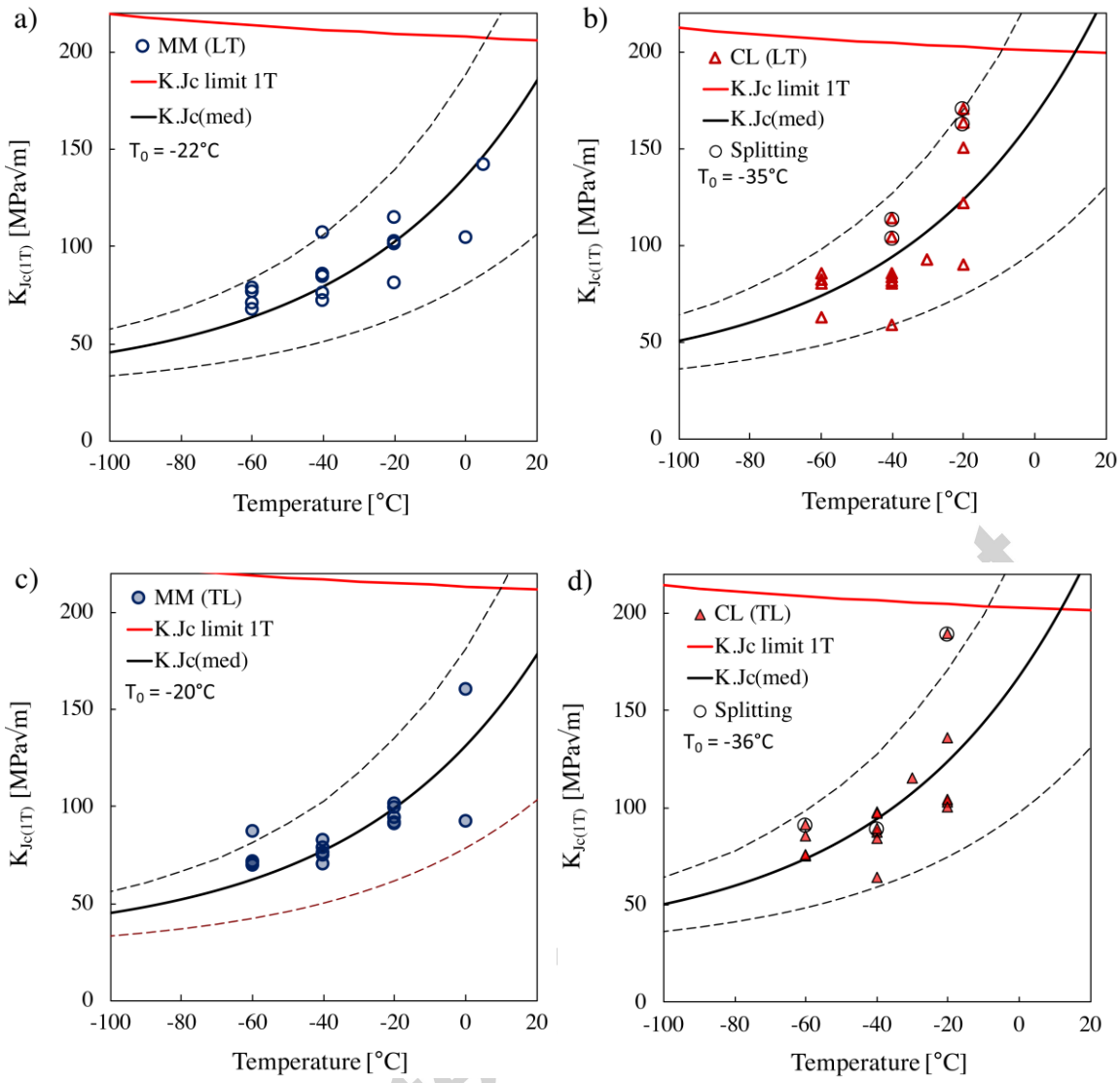

Fig. 2. Fracture toughness test results as $K_{Jc(1T)}$ with Master Curve fits and their 95% confidence limits of a) MM (LT), b) CL (LT), c) MM (TL) and d) CL (TL).

3.2. Microstructure, chemical composition and hardness

The microstructures of both materials are through-hardened as-quenched martensite. The microstructure of the material MM is approximately 90% auto-tempered lath martensite containing clearly visibly carbides and 10% untempered lath martensite with at most only very weakly visible carbides as shown in Fig. 3 a). Material CL is 85% auto-tempered lath martensite and 15% untempered lath martensite (Fig. 3 b). No residual austenite was found in the XRD measurements, which in practice means that the content is less than 1 percent and, if present, are likely very finely distributed [45].

In the following analyses, we divide CL thickness-wise into the middle third, i.e. ± 2 mm from the plate centreline, and the upper and lower thirds, i.e. those parts > 2 mm from the plate centreline. MM appears homogeneous through its thickness and is presented undivided.

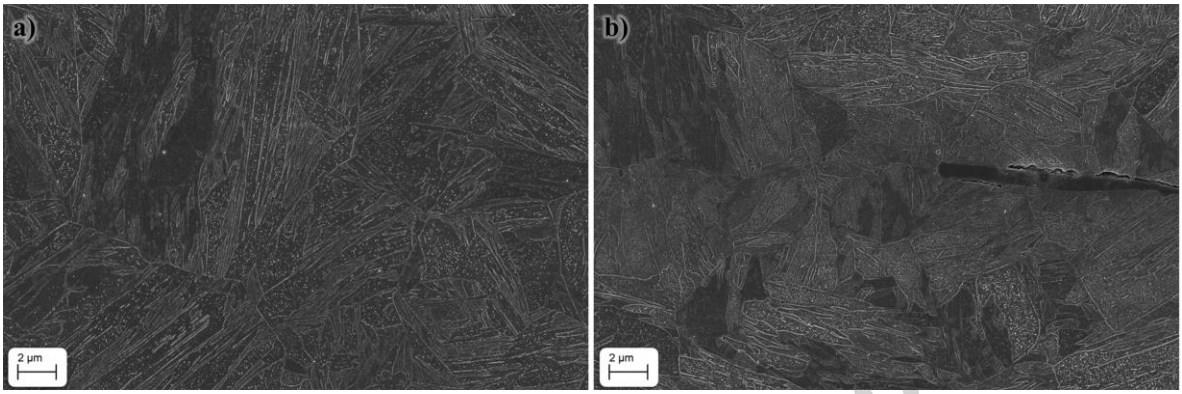

Fig. 3. Microstructures at the plate centreline of the materials a) MM, b) CL with a MnS inclusion.

Table 2 shows the main alloying elements and their variation between the materials and through the thickness with the estimated hardness values calculated using Eq. [1]. In addition to those shown, the following elemental concentrations in wt.% were measured (MM / CL): Al 0.03 / 0.03, Ca 0.003 / 0.002, O 0.002 / 0.002, N 0.005 / 0.005 and Ni 0.05 / 0.06. At the bulk level, the materials show only the slightest differences in chemical composition that account for only six HV units difference in the estimated hardness calculated after Blondeau et al. [42]. That is well in line with the measured average through-thickness HV_{10} hardness of 391 (± 2) and 395 (± 3) of the materials MM and CL, respectively.

Differences in chemical composition appear when the normal planes from different depths are studied with GD-OES. While the upper and lower thirds of CL are similar to MM, the middle third of CL shows clear segregation. The alloying elements drawn into the centreline boost its hardenability and deplete the regions adjacent to the

centreline segregation of alloying elements. The enrichment increases the estimated hardness 27 HV on average and 45 HV based on the maximum concentration. These variations coincide accurately with the measured hardness: the scatter is low in MM with the values falling in the range [375,402] HV_{10} (Fig. 4 a) whereas CL shows substantial scatter through the thickness with the range [367,448] HV_{10} (Fig. 4 b).

Zooming in to the middle third of the materials with EPMA, the banded nature of the segregation emerges (Fig. 5) with a through-thickness variation of Mn, Cr and Mo. Yet again, the scatter in MM is minor (Fig. 5 a), though existing, compared to the fluctuation in CL, where six to seven peaks corresponding to segregation bands can be recognised (Fig. 5 b).

Table 2. The chemical compositions (wt.%) as measured with SS-OES (bulk) and the percentual differences with 95% confidence intervals on different depths (mm) from the plate centrelines as measured with GD-OES.

Material	C	Mn	Cr	Mo	Ti	S	Est. HV_M (Eq. [1])
MM (bulk)	0.124	1.080	0.705	0.155	0.030	0.002	389
MM (4)	-4.0 (± 0.8)	+13.6 (± 1.2)	+6.5 (± 0.8)	+25.2 (± 1.5)	+23.3 (± 5.4)	+57.9 (± 6.7)	387
MM (0)	-3.2 (± 0.8)	+14.3 (± 0.8)	+7.0 (± 0.5)	+26.5 (± 1.0)	+30.0 (± 2.6)	+57.9 (± 10.0)	388
CL (bulk)	0.130	1.100	0.709	0.157	0.032	0.002	395
CL (4)	-5.3 (± 6.5)	+6.9 (± 5.6)	+4.1 (± 8.0)	+17.9 (± 7.6)	+12.39 (± 8.3)	+103.3 (± 19.5)	390
CL (2)	-9.1 (± 0.8)	+19.8 (± 0.3)	+24.8 (± 1.4)	+31.89 (± 6.5)	+28.4 (± 17.1)	-15.0 (± 11.8)	390
CL (0)	+17.9 (± 3.9)	+19.4 (± 3.3)	+17.8 (± 4.4)	+32.19 (± 2.9)	+45.6 (± 10.6)	+86.1 (± 10.8)	422
CL (max)	+30.2 (± 0.1)	+31.7 (± 2.6)	+29.1 (± 1.4)	+45.09 (± 3.1)	+99.8 (± 10.9)	+105.0 (± 24.4)	440

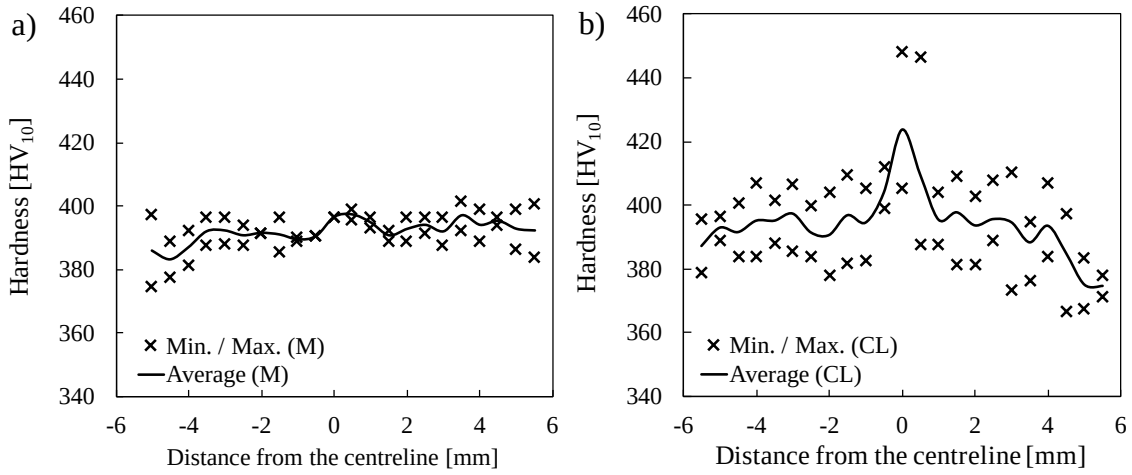

Fig. 4. Hardness profiles of the materials a) MM and b) CL.

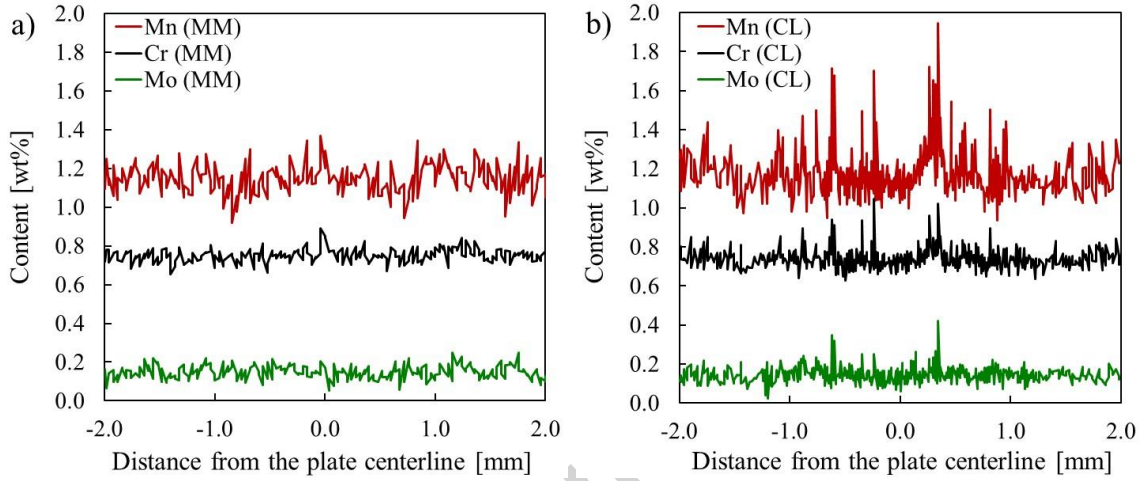

Fig. 5. The local through-thickness variation of elements Mn, Cr and Mo as measured with EPMA in a) MM and b) CL.

3.3. Inclusions

We divide the mapped inclusions into four different groups based on the main element: aluminium, calcium, manganese and titanium. Within these groups, there are nitrides, oxides, sulphides and mixed types. These mixed inclusions with secondary particles are grouped together by equivalent circle diameter and appearance, where appropriate. The total number of mapped inclusions is 3651 in the material MM and 3293 in the material CL. From Fig. 6 a) and b) it is evident, that CL possesses larger inclusions, with the exception of CaOS, which are 23% bigger in the material MM. Especially MnS based inclusions are clearly larger in CL. The mixed inclusions that contain TiN as a secondary

particle are notably smaller compared to otherwise similar Al, Ca and MnS based inclusions without the presence of TiN (Fig. 6 a).

Comparing inclusion size distributions (Fig. 6 b), MM has a higher frequency of smaller inclusions (< 2 µm), 70% of its population, whereas the majority of the mapped inclusions in CL are larger than 2 µm. The middle section, which is where the brittle failure generally nucleates, contains most of the large inclusions (69%) in CL. The size of the largest inclusions at 80% of the cumulative distribution ($d_{i\text{-}80\%}$) is 3.3 µm for MM and the upper and lower thirds of CL but 5.3 µm for the middle third of CL.

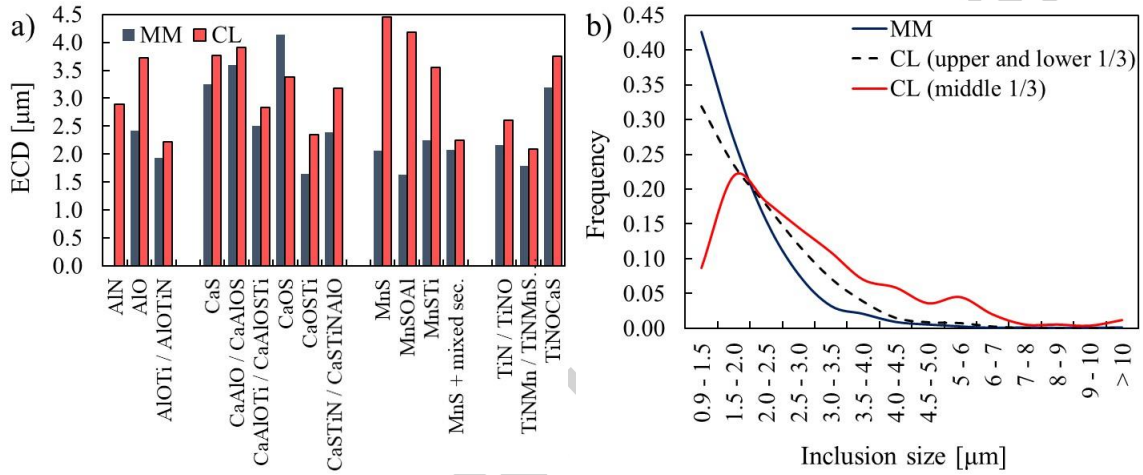

Fig. 6. a) The inclusion types with their respective average equivalent circle diameters (ECD), b) inclusion sizes in MM and in CL, with CL also divided into thickness-wise thirds.

3.4. Grain size

The prior austenite grain structures separate the two materials further (Fig. 7). The material MM has a quite uniform grain size distribution with some distinct larger grains as can be seen from the micrographs in Fig. 7 a) and c) and the grain size distributions in Fig. 8 a). On the other hand, the material CL contains frequent segregation bands (Fig. 5 b), of which a representative example shows a bimodal grain size distribution containing both fine grained and coarse grained areas, Fig. 7 b), d) and Fig. 8 a). These segregation

bands possess significantly smaller PAGS (prior austenite grain size), but also a concentration of large inclusions, Fig. 3 b), Fig. 7 b).

The fine-grained segregation bands result in a laminar-like structure with a smaller mean PAGS of 5.9 µm for the middle third of CL (Table 3), compared to the outer thirds. Those have a bimodal distribution, which consists of a peak from the segregation bands and a peak of larger grains between the bands (Fig. 8 a). The peak of MM falls between these two. Consequently, MM and the outer sections of CL have the same mean PAGS of 8.9 µm (Table 3).

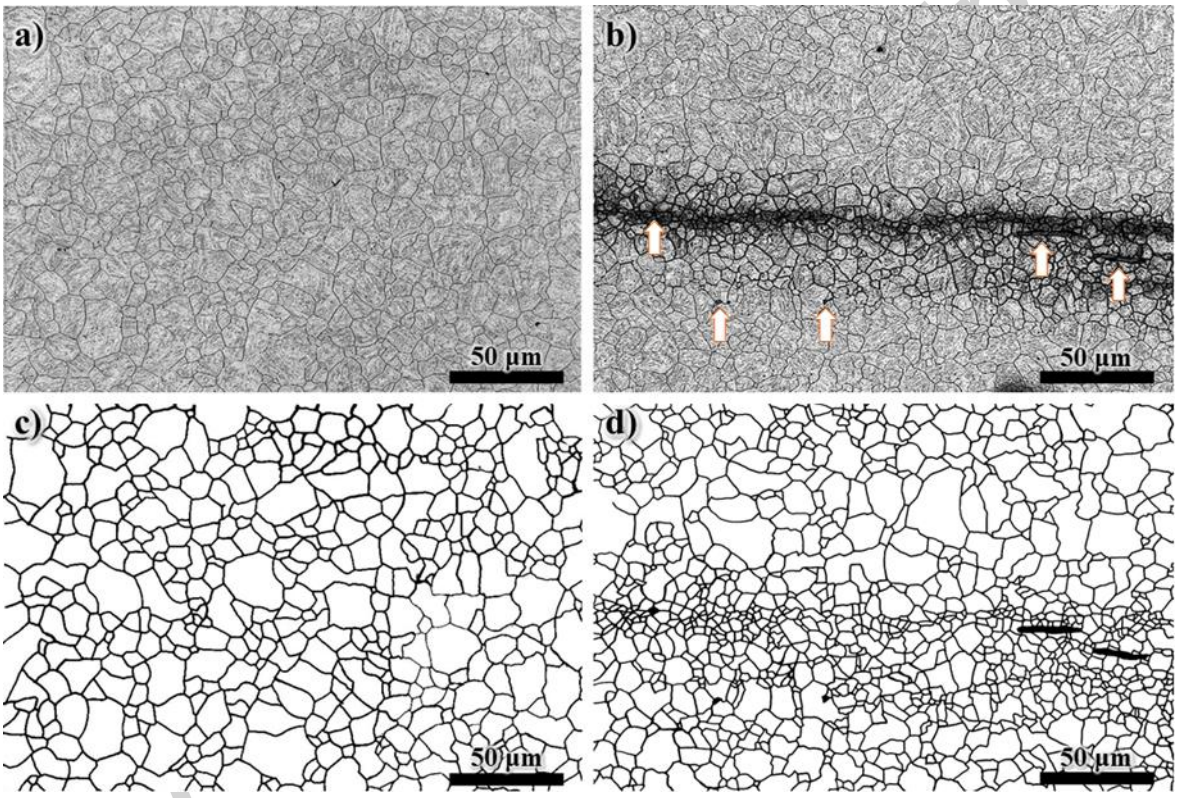

Fig. 7. The prior austenite grain structure in materials MM and CL, the latter with a representative segregation band in the plate centreline, as nital-etched and imaged with a laser microscope in a) and b), and binarised images showing the grain boundaries in c) and d), respectively. The arrows in b) point to inclusions.

Advancing to the measures of effective grain size of the martensite, i.e. the size of grains surrounded by boundaries with a misorientation > 15° as measured using EBSD,

we see that the size of the coarsest grains at the 80th percentile position in the grain size distribution, $d_{80\%}$ - a measure of the effective coarse grain size d_{ecgs} [37], is slightly finer in the outer thirds of CL compared to MM, and significantly smaller in the central third of CL (Fig. 8 b). Emphasising this, the differences in $d_{80\%}$ is 43% between MM and the middle section of CL (Table 3). The average grain sizes for both the MM material and all thirds of the CL material is of the order of 1 µm (Table 3).

In some microstructures, carbide sizes are known to influence cleavage crack nucleation [10]. In the present microstructures, the carbides are significantly, although only marginally, larger in the middle third of CL than in MM (Table 3). The carbide size of the outer thirds of CL is between those two. As with grain size, carbide size is defined as the ECD. For both materials, the coarse carbide size ($d_{carb\text{-}80\%}$) is around 40 nm and the biggest observed carbides in both materials are < 100 nm ECD.

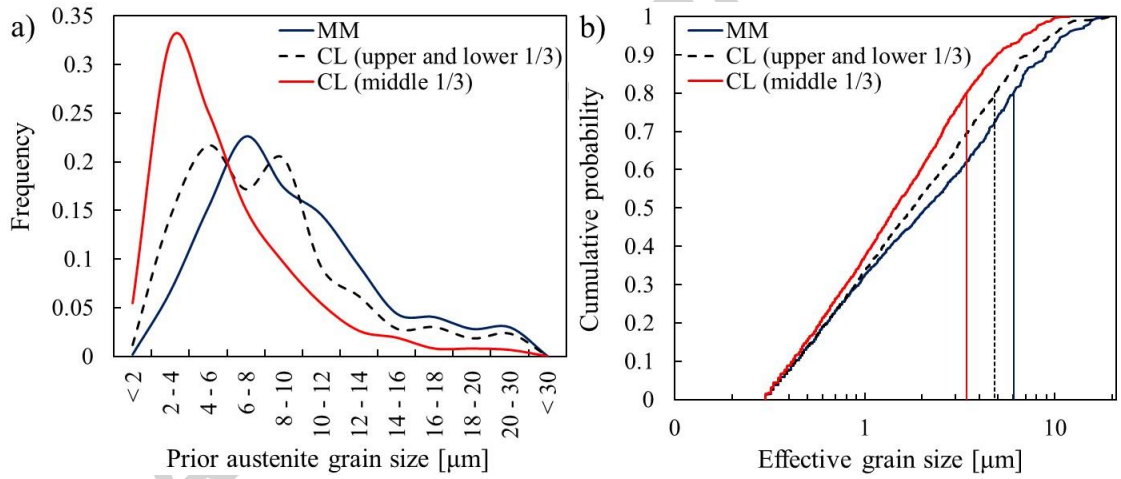

Fig. 8. a) Prior austenite grain size in MM and in the different thirds of CL. b) Cumulative probabilities of the effective grain size in MM and CL highlighting the effective coarse grain size $d_{80\%}$.

Table 3. Grain size parameters and carbide size. (PAGS = prior austenite grain size, effective grain size parameters (> 15° misorientation) d_{avg} = average effective grain size and $d_{80\%}$ = effective coarse grain size, and $d_{carb\text{-}80\%}$ = coarse carbide size).

Material (section)	PAGS [µm]	d_{avg} [µm]	$d_{80\%}$ [µm]	Carbide size [nm]	$d_{carb\text{-}80\%}$ [nm]
M	8.9 (± 0.1)	1.16 (± 0.06)	6.05	18.5 (± 1.6)	40.0
CL (upper and lower 1/3)	8.9 (± 0.2)	1.11 (± 0.04)	4.80	22.1 (± 2.3)	39.3
CL (middle 1/3)	5.9 (± 0.2)	1.00 (± 0.03)	3.43	23.2 (± 0.8)	39.3

3.1. Fractography

Overall, the fracture surfaces of both the SENB and CVN specimens are typical of ferritic materials tested in the DBTT range, consisting of mixed brittle areas separated by frequent narrow ductile stretches. The macroscopic fracture surfaces of the material MM at -20 °C and below are essentially flat, whereas CL specimens frequently possess either one large or one to three smaller splits (Fig. 9).

We investigated 43 CVN and SENB specimens tested in the DBTT region under microscopes. In 56% of the cases the primary cleavage fracture initiator (CI) could be identified (Table 4). Those specimens in which no CI could be identified, contained multiple initiation regions due to either excessive brittleness, large splits and/or ductile crack growth. Large TiN and CaOS inclusions (Fig. 6 a, Fig. 10 a) or clusters followed by grain boundary triple points are the most common CI in the material MM. Abundant TiN and Ca-based inclusions could be found near the local failure initiation sites in MM. TiN inclusions are the dominant crack initiation sites in the CL material, either as a large individual inclusion (Fig. 10 b) or as a cluster. The TiN inclusions at the nucleation sites in CL either appeared alone or they were accompanied by MnS (Fig. 10 d). No evidence of carbide-initiated failure was found.

The average ECD sizes of the inclusions initiating cleavage cracks are 4.6 ± 0.8 µm and 7.4 ± 1.8 µm for the materials MM and CL, respectively. These correspond to the

94th and 90th percentiles in the cumulative size distributions. The average cleavage fracture unit sizes around the primary initiation sites are 5.8 ± 0.6 μm and 5.6 ± 0.4 μm for MM and middle third of CL, which correspond to the 79th and 92nd percentile, respectively.

The splits, which are present only in CL, start with an inclusion, either straight from the pre-fatigued crack tip or after a short stretch of ductile crack growth, and contain very large MnS inclusions, up to 30 μm long as measured in the main fracture plane. The split morphologies are diverse with two examples shown in Fig. 9 b & Fig. 10 c. The bottoms of the splits, where observable, always exhibit transgranular cleavage. The sides of the splits are mainly a combination of cleavage fracture and multi-void coalesced (MVC) ductile fracture with a strong division between the "left and right" sides of V-shaped splits when only one half of a specimen is considered, Fig. 9 b) and Fig. 10 c). The side that has supposedly formed first has failed by cleavage and the latter side by MVC. Shear lips were present on most of the splits (Fig. 10 c), but in some instances, the tops of smaller splits were flat without shear lips. In both LT and TL oriented specimens, large inclusions infest the walls of the splits (Fig. 10 d) showing that inclusion clusters spread in the rolling direction play a role in split formation. As measured in the main fracture plane, the splits are longer in the TL oriented specimen than in TL, which reflects the length of the segregation bands on the given crack planes.

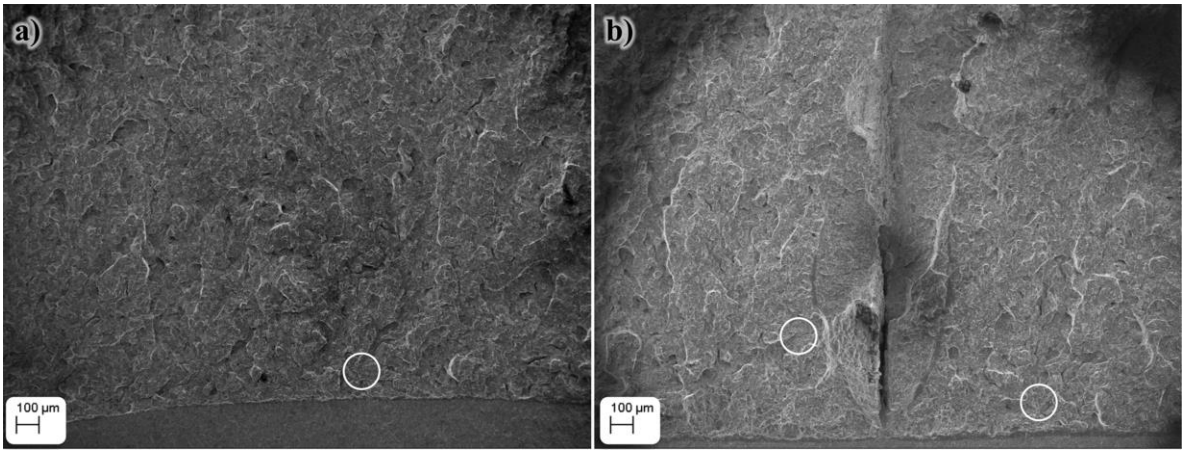

Fig. 9. Typical crack propagation in TL oriented SENB specimen of a) MM and b) CL with a split. Circles show cleavage fracture initiation sites.

Table 4. The primary failure initiators in SENB and CVN specimens and the number of specimens with macroscopic splits. (+) denotes the presence of secondary components in the inclusions.

	M (SENB)	M (CVN)	CL (SENB)	CL (CVN)
Total number examined	13	5	13	12
CaOS(+) / CaOS cluster	3	0	0	0
TiN(+) / TiN cluster	2	2	5	2
TiN(+) and MnS	0	0	1	2
Grain boundary triple point	2	1	0	0
Unidentified	6	2	7	8
Macroscopic splitting (LT / TL)	0 / 0	0 / 0	4 / 2	2 / 8

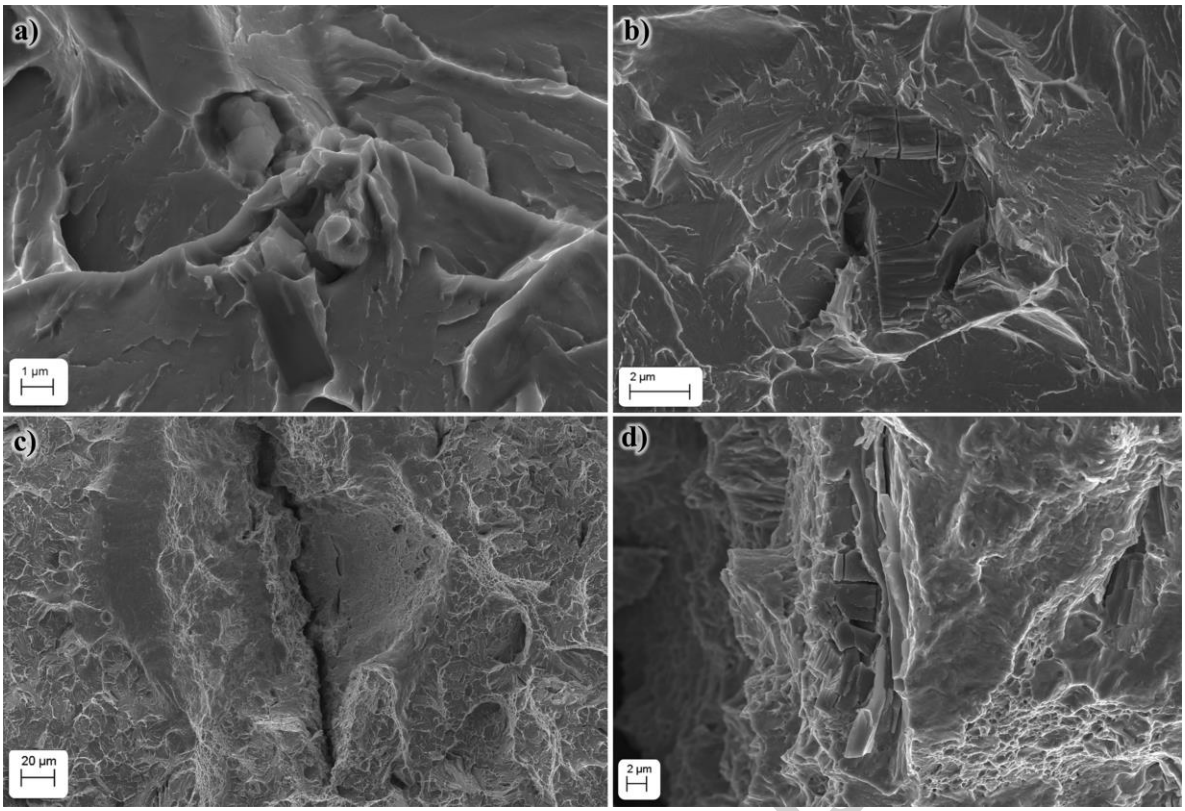

Fig. 10. Inclusions contributing to crack propagation: a) TiN & CaOS that have nucleated a local cleavage fracture in MM CVN specimen, b) a large TiN that has initiated the failure in a CL SENB specimen without splits, c) split morphology in CL showing a shear lip and a brittle and a ductile side, and d) TiN inclusions & MnS at the apex of a large split (CL, SENB).

4. DISCUSSION

The fact that the "dirty" inclusion rich and heterogeneous CL material is more resistant to failure initiation in the DBTT regime than the "clean" homogeneous MM material is, at first sight, unexpected: the CL material is associated with a plate centreline that is 15% harder than the MM material, i.e. harder by 60 HV_{10} units, and the large inclusions at the 80th percentile of the cumulative size distribution are 60% coarser in the CL specimens than in the MM specimens. However, the tougher behaviour of the CL material can be explained by the finer local effective coarse grain size, which is especially pronounced in the laminar-like plate centreline in hard, inclusion rich segregation bands (Fig. 7). The fine grain size seems to counteract the detrimental effects expected from the presence of

larger and more numerous inclusions and a higher hardness. According to JMatPro calculations, the enrichment in the hardening elements [6] and the decrease in PAGS [46] cause the martensite start and martensite finish temperatures to drop by approximately 50 °C at the plate centreline of CL, which is seen as a slightly higher fraction of untempered martensite due to the lower transformation temperatures and shorter time for auto-tempering. Considering hardness and excluding the changes in residual stresses, this difference in the martensite start and stop temperatures appears to be negligible, as the hardness at different thicknesses follow the estimates of Eq. [1] accurately.

PAG size is an important parameter as it determines the upper limit of the effective coarse grain size the final microstructure can possess and thus affects the resulting DBTT [37,47,48]. The finer PAG size in the segregation bands is presumably due to a higher density of grain growth hindering precipitates in the reheated austenite prior to the final quenching. The nature of these precipitates has not been examined here, but it is not unreasonable to suppose that they are TiN that have a higher number density and stronger retarding effect on grain growth due to the segregation of Ti and N along with the main alloying elements during solidification. It is also likely that grain growth will be retarded more in the segregated bands by a higher solute drag arising from the enrichment of the main alloying elements [6].

In the fracture toughness specimens of the homogeneous MM, the measured size of the cleavage fracture units around the failure initiation sites coincides with the effective grain size at the 80^{th} percentile of the cumulative effective grain size distribution, implying that this is the statistically appropriate level for assessing the fracture toughness in the transition temperature region. With the heterogeneous CL material, it coincides with the 92^{nd} percentile of the cumulative effective grain size distribution of the middle third. Note that the actual unit size is the same (5.6 – 5.8 μm) in both materials. This is

simply due to the same critical stress criterion they are both exposed to, while the sampling of a critically sized weakest links is probable enough in both materials.

In the cases studied (Table 4), crack initiation from inclusions was more common than initiation at other sites, namely grain boundary triple points. The average sizes of these inclusions coincide with the 94th percentile (MM: 4.6 μm) and 90th percentile (CL: 7.4 μm) in the cumulative size distributions, and they are surrounded by the large grains with sizes at the abovementioned 80% and 92% levels. In order to initiate a failure, a large brittle unit needs to be located in a coarse-grained matrix within the highly stressed process zone to propagate the microcrack far enough to accumulate a critical level of damage. This is a double-barrier criterion [15] where the first barrier is the inclusion - grain interface and the second barrier the boundary between coarse grains. The broken large inclusions found in a ductile matrix inside the fracture process zone back up the importance of the size of the surrounding grains (Fig. 11).

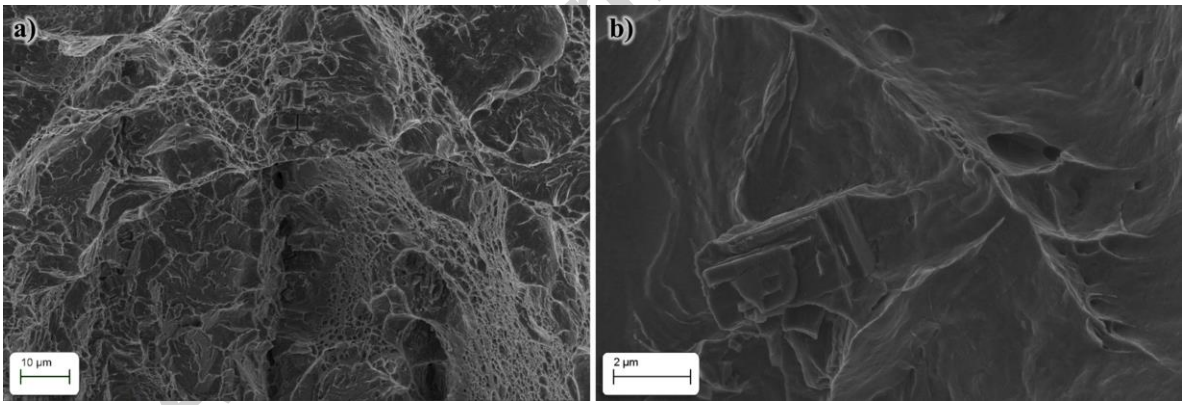

Fig. 11. Broken inclusions surrounded by a ductile matrix found close to the primary failure initiator in CL.

To further evaluate the critical large units, we utilised a simple Griffith crack criterion [49], Eq. [2]. A common feature of the analyses of cleavage crack initiation from small carbides and larger inclusions is that they utilise a low stress concentration factor f applicable to the propagation of a through-thickness crack, i.e. $f = 4/\pi \approx 1.273$

[3,8–10,13,21]. In addition to this, there has been lack of direct evidence relating carbides to the primary cleavage crack origin [3].

$$\sigma_f = \sqrt{f \times \frac{E\gamma_{eff}}{(1-\upsilon^2)d}} = \sqrt{\frac{\pi E\gamma_{eff}}{(1-\upsilon^2)d}} \quad [2]$$

The macroscopic crack tip will influence the stress intensity at a microcrack that forms ahead of it. As a result, the critical fracture stress for a penny-shaped crack in front of a macroscopic crack gets the form of Eq. [2] below with f = π[5,14,19,49]. Using an effective surface energy of 100 J/m^2 for the given DBTT [50] and setting the failure criterion to $\sigma_f \approx 3\times\sigma_{YS}$, which is appropriate for small-scale yielding in a non-hardening material, the results are in line with the experimental findings as shown by Fig. 12 (where the average σ_{YS} of CL is applied to both the middle third and the outer thirds). For the "clean" homogeneous MM, the effective coarse grain sizes $d_{80\%}$ and $d_{90\%}$ are around the criterion level but the failure initiating inclusions are slightly above it. After a suitably large inclusion is sampled in the process zone, it is easy for the crack to propagate through the large-grained matrix (MM, outer 1/3s of CL). In the middle third of the "dirty" inclusion rich heterogeneous CL, an average large inclusion meets the criterion with ease, especially inside the segregation bands, but its propagation is more difficult due to the smaller effective coarse grain size.

Because the probability of encountering a cleavage crack that is large enough to propagate and produce a detectable drop in the load-displacement curve is lowered by the segregation in an otherwise very unfavourable environment, the brittle fracture toughness K_{Jc} is elevated. We illustrate this with Fig. 13, which shows coarse grains at the plate centreline of the homogeneous MM (Fig. 13 a) and very fine grains surrounding MnS and TiN inclusions (Fig. 13 b) in a segregation band of the heterogeneous CL.

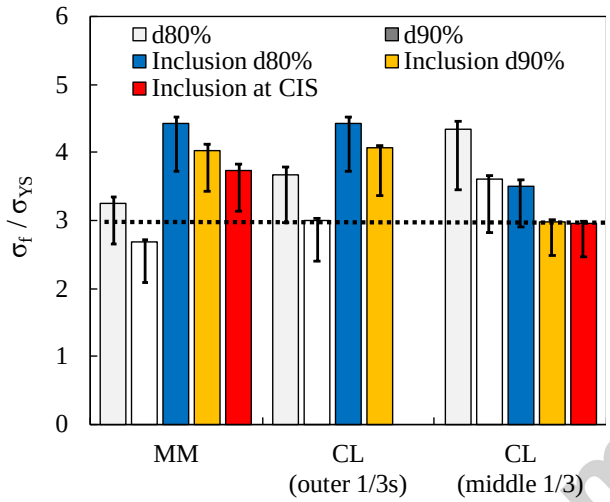

Fig. 12. The relative critical failure stress according to the modified Griffith criterion using static yield stress values corrected to -40 °C. The upper limits of the bars show the situation for static yield stress corrected to -20 °C, i.e. in the region of T_0, and the lower limits of the bars correspond to dynamic yield stress values at a strain rate of 10^{-3} s^{-1} and -40 °C, i.e. the region of T_{28J}.

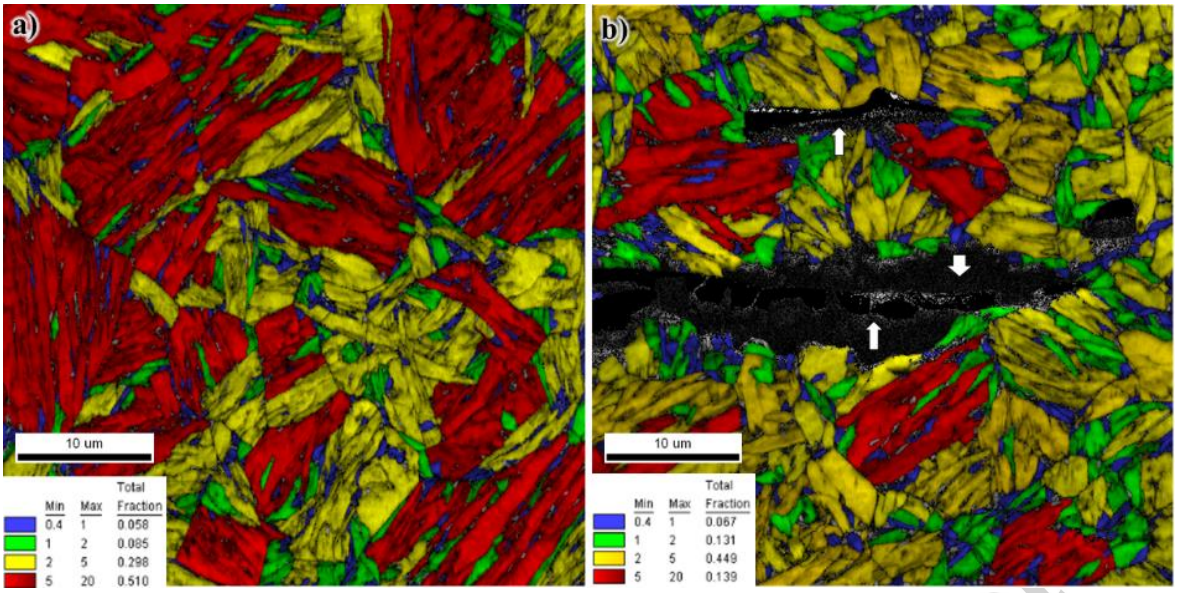

Fig. 13. The grain size distribution in the plate centreline of materials a) MM and b) CL around inclusions. The white arrows pointing upwards indicate MnS inclusions and the arrow pointing downwards a TiN inclusion accompanied by a large MnS inclusion. The insets give the colour coding of the ECD grain sizes in microns. For colours, the reader is referred to the online version of the paper.

Large TiN-based inclusions are clearly the most important initiators of low-temperature fractures in these materials accounting for 70% of the identified causes of the primary failures. In fracture toughness testing, T_0 is unaffected by the specimen orientation; but in the case of Charpy V impact toughness testing, inclusions spread in the rolling direction lower the impact toughness of the TL oriented specimens. Inclusion stringers lower the resistance to crack propagation in TL oriented specimens compared to LT oriented specimens. This accounts for the higher T_{28J} transition temperatures of the TL specimens: 11 °C in the case of the MM material and 21 °C for the CL material. The greater effect of inclusion stringers on crack propagation in the case of the CL material is also seen in the CVN fracture surfaces, which show more frequent and longer stringers.

In the transition region, the inclusions have a dual role in the heterogeneous microstructure. Large TiN-based inclusions can nucleate splits (Fig. 10 c), and on the basis of the frequency of inclusions on the exposed split walls, the splits also propagate

along the lines of elongated inclusion stringers (Fig. 10 d). The CVN specimens showing splits after testing at -60 °C absorbed more energy than those that were without splits (Fig. 1 b). This caused scatter in the measured toughness values [22,24,28]. The same effect is visible in the fracture toughness test results, Fig. 2 b) and d), where the SENB specimens with smaller non-critical splits formed before the failure have higher K_{JC} than the specimens without splits. This difference is 40 % (+31 to +46 MPa$\sqrt{m}$) in the LT orientation at -20 °C and -40 °C, but varies strongly in TL orientation from +7 to +75 MPa$\sqrt{m}$. Large splits have formed either at or after the failure point in the fracture toughness tests. While the inclusions that nucleate the primary failure are cracked, most of the inclusions on the walls of the splits show at least partial debonding (Fig. 10 d). This applies especially to MnS inclusions, which appear to promote split propagation by being both longer in the rolling direction and easily debondable. The non-criticality of large MnS inclusions as a primary cleavage fracture initiator can be due to their tendency to debond already during cooling because MnS has a higher coefficient of thermal expansion than the steel matrix, thereby forming blunter voids. However, the opposite applies for stress-raisers like CaOS and TiN based inclusions that have smaller coefficients of thermal expansion than the steel matrix [51].

5. CONCLUSIONS

We investigated the microstructural features affecting the impact and fracture toughness of as-quenched martensite in the ductile-brittle transition temperature region of 12 mm thick homogeneous and heterogeneous steel plates that were produced in the laboratory by hot rolling samples extracted from the same continuously cast slab. The homogeneous material was free of macrosegregation while the heterogeneous material showed strong centreline segregation and a high density of large inclusions in the middle third of its

thickness. The tensile properties of the two materials were the same, and the impact toughness transition temperatures T_{28J} did not show significant differences. However, despite having a strongly segregated microstructure with very hard, inclusion rich bands, the heterogeneous "dirty" material possessed a significantly better fracture toughness transition temperature T_0. The reasons for this behaviour are as follows:

- When compared to the clean homogeneous material, the inclusion rich segregated material has a drastically smaller prior austenite grain size giving the transformed martensite a 43% smaller effective coarse grain size at the 80th percentile of the cumulative distribution. This lowers the probability of finding a cleavage crack nucleating inclusion in a large grained matrix and improves the brittle fracture toughness of the "dirty", inclusion rich, heterogeneous material.
- Since fractography shows that the main failure initiation sites are the coarsened regions outside the inclusion rich segregation bands, we conclude that the locally very fine grain size of the segregation bands protects the material from cleavage crack propagation in these otherwise vulnerable regions.
- The fact that the main cleavage crack initiation sites contained the coarsest inclusions and the coarsest grains, with sizes corresponding to the 80th – 90th percentiles in the respective size distributions, indicates that the weakest link pair with regard to primary failure is a coarse inclusion that is surrounded by coarse grains. In the "clean" homogeneous material, the critical inclusions are large individuals or stringers of TiN and CaOS. In the inclusion rich heterogeneous material, the critical inclusions are TiN particles, either alone or in combination with large MnS inclusions.

- Splitting increases absorbed energy in the transition region. The nucleation of the split is associated to coarse TiN (and MnS) based inclusions. Elongated extraordinarily large MnS and TiN clusters promote the propagation of the splits. Small splits that do not determine the failure point in the fracture toughness test increase the fracture toughness of the heterogeneous material. Larger splits either determine the failure point or form after the failure and so do not improve toughness.

Acknowledgements

The authors gratefully acknowledge the funding provided through the BSA programme of DIMECC Ltd. from the Finnish Funding Agency for Innovation (Tekes) and the participating companies, and from the Academy of Finland for the project Genome of Steel (311934). Dr. Pallaspuro would also like to thank the Association of Finnish Steel and Metal Producers, the Finnish Foundation for Technology Promotion (TES) and the University of Oulu Graduate School for financially supporting the visit to NTNU. SSAB is thanked for providing experimental raw materials and for conducting the mechanical testing. We are grateful to Dr. Tuomo Saarinen for the EDS inclusion mapping. From the University of Oulu, Dr. Jarkko Puustinen and Mr. Pasi Juntunen are thanked for the XRD measurements, and Mrs. Leena Palmu for operating the EPMA.

Data availability

The raw/processed data required to reproduce these findings cannot be shared at this time due to technical or time limitations.

References

[1] D.A. Porter, K.E. Easterling, M.Y. Sherif, Phase transformations in metals and alloys, 3rd ed., CRC Press, 2009.

[2] Y. Tomita, Improved fracture toughness of ultrahigh strength steel through control of non-metallic inclusions, J. Mater. Sci. 28 (1993) 853–859. doi:10.1007/BF00400864.

[3] A. Echeverría, J.M. Rodriguez-Ibabe, Brittle fracture micromechanisms in bainitic and martensitic microstructures in a C-Mn-B steel, Scr. Mater. 41 (1999) 131–136. doi:10.1016/S1359-6462(99)00124-4.

[4] M. Mäntylä, A. Rossoll, I. Nedbal, C. Prioul, B. Marini, Fractographic observations of cleavage fracture initiation in a bainitic A508 steel, J. Nucl. Mater. 264 (1999) 257–262. doi:10.1016/S0022-3115(98)00496-6.

[5] W.W. Bose Filho, A.L.M. Carvalho, P. Bowen, Micromechanisms of cleavage fracture initiation from inclusions in ferritic welds. Part I. Quantification of local fracture behaviour observed in notched testpieces, Mater. Sci. Eng. A. 460–461 (2007) 436–452. doi:10.1016/j.msea.2007.01.115.

[6] H.K.D.H. Bhadeshia, R.W.K. Honeycombe, Steels - Microstructure and Properties, 3rd ed., Elsevier, Oxford, 2006.

[7] K. Wallin, M. Yamamoto, U. Ehrnstén, Location of initiation sites in fracture toughness testing specimen - The effect of size and side grooves, in: Proc. ASME 2016 Press. Vessel. Pip. Conf., ASME, Vancouver, 2016: pp. 1–9.

[8] P. Bowen, S.G. Druce, J.F. Knott, Micromechanical modelling of fracture toughness, Acta Metall. 35 (1987) 1735–1746. doi:10.1016/0001-6160(87)90119-2.

[9] X.Z. Zhang, J.F. Knott, Cleavage fracture in bainitic and martensitic microstructures, Acta Mater. 47 (1999) 3483–3495. doi:10.1016/S1359-6454(99)00200-1.

[10] S. Lee, S. Kim, B. Hwang, B.S. Lee, C.G. Lee, Effect of carbide distribution on the fracture toughness in the transition temperature region of an SA 508 steel, Acta Mater. 50 (2002) 4755–4762. doi:10.1016/S1359-6454(02)00313-0.

[11] K. Wallin, A. Laukkanen, New developments of the Wallin, Saario, Törrönen cleavage fracture model, Eng. Fract. Mech. 75 (2008) 3367–3377. doi:10.1016/j.engfracmech.2007.07.018.

[12] H. C. H.C., The Importance of the Non-Metallic Inclusions in Steel, Nature. 101 (1918) 334–335. http://www.nature.com/nature/journal/v101/n2539/pdf/101334a0.pdf.

[13] P. Bowen, J.F. Knott, Cleavage fracture of A 533 B pressure vessel steel in martensitic condition, Met. Sci. 18 (1984) 225–235. doi:10.1179/030634584790420131.

[14] W.W. Bose Filho, A.L.M. Carvalho, P. Bowen, Micromechanisms of cleavage fracture initiation from inclusions in ferritic welds Part II. Quantification of local fracture behaviour observed in fatigue pre-cracked testpieces, Mater. Sci. Eng. A. 452–453 (2007) 401–410. doi:10.1016/j.msea.2007.01.115.

[15] A. Lambert-Perlade, A.F. Gourgues, J. Besson, T. Sturel, A. Pineau, Mechanisms and modeling of cleavage fracture in simulated heat-affected zone microstructures of a high-strength low alloy steel, Metall. Mater. Trans. A. 35 (2004) 1039–1053. doi:10.1007/s11661-004-1007-6.

[16] B. Hwang, C.G. Lee, S.-J. Kim, Low-Temperature Toughening Mechanism in Thermomechanically Processed High-Strength Low-Alloy Steels, Metall. Mater. Trans. A. 42 (2011) 717–728. doi:10.1007/s11661-010-0448-3.

[17] J.W. Morris, Jr., On the Ductile-Brittle Transition in Lath Martensitic Steel, ISIJ Int. 51 (2011) 1569–1575. doi:10.2355/isijinternational.51.1569.

[18] J. Han, A.K. da Silva, D. Ponge, D. Raabe, S.-M. Lee, Y.-K. Lee, S.-I. Lee, B. Hwang, The effects of prior austenite grain boundaries and microstructural morphology on the impact toughness of intercritically annealed medium Mn steel, Acta Mater. 122 (2017) 199–206. doi:10.1016/j.actamat.2016.09.048.

[19] J. Du, M. Strangwood, C.L. Davis, Effect of TiN Particles and Grain Size on the Charpy Impact Transition Temperature in Steels, J. Mater. Sci. Technol. 28 (2012) 878–888. doi:10.1016/S1005-0302(12)60146-7.

[20] A. Ghosh, A. Ray, D. Chakrabarti, C.L. Davis, Cleavage initiation in steel: Competition between large grains and large particles, Mater. Sci. Eng. A. 561 (2013) 126–135. doi:10.1016/j.msea.2012.11.019.

[21] R. Cao, G. Li, X.Y. Fang, J. Song, J.H. Chen, Investigation on the effects of microstructure on the impact and fracture toughness of a C-Mn steel with various microstructures, Mater. Sci. Eng. A. 564 (2013) 509–524. doi:10.1016/j.msea.2012.11.120.

[22] Z. Sterjovski, D.P. Dunne, D.G. Carr, S. Ambrose, The Effect of Cold Work and Fracture Surface Splitting on the Charpy Impact Toughness of Quenched and Tempered Steels, ISIJ Int. 44 (2004) 1114–1120.

[23] R. Punch, M. Strangwood, C. Davis, Origin and propagation of splits in high-strength low-alloy strip steel, Metall. Mater. Trans. A Phys. Metall. Mater. Sci. 43 (2012) 4622–4632. doi:10.1007/s11661-012-1307-1.

[24] M.S. Joo, D.-W. Suh, J.H. Bae, H.K.D.H. Bhadeshia, Role of delamination and crystallography on anisotropy of Charpy toughness in API-X80 steel, Mater. Sci. Eng. A. 546 (2012) 314–322. doi:10.1016/J.MSEA.2012.03.079.

[25] X.J. Shen, S. Tang, Y.J. Wu, X.L. Yang, J. Chen, Z.Y. Liu, R.D.K. Misra, G.D. Wang, Evolution of microstructure and crystallographic texture of microalloyed steel during warm rolling in dual phase region and their influence on mechanical properties, Mater. Sci. Eng. A. 685 (2017) 194–204. doi:10.1016/J.MSEA.2016.12.108.

[26] E. Maina, D.N. Crowther, J.R. Banerjee, B. Mintz, Influence of directionality on strength and impact behaviour of high strength steels, Mater. Sci. Technol. 28 (2012) 390–396. doi:10.1179/1743284711Y.0000000061.

[27] K. Wallin, Fracture Toughness of Engineering Materials - Estimation and Application, EMAS Publishing, Warrington, 2011.

[28] M. Yang, Y.J. Chao, X. Li, D. Immel, J. Tan, Splitting in dual-phase 590 high strength steel plates Part II. Quantitative analysis and its effect on Charpy impact energy, Mater. Sci. Eng. A. 497 (2008) 462–470.

[29] J. Kömi, P. Karjalainen, D. Porter, Direct-Quenched Structural Steels, in: Encycl. Iron, Steel, Their Alloy., CRC Press, 2016: pp. 1109–1125. doi:10.1081/E-EISA-120049737.

[30] CEN, EN 1993-1-12, Eurocode 3, Design of steel structures - Part 1-12: Additional rules for the extension of EN 1993 up to steel grades S 700, CEN - European Committee for Standardization, 2007. http://docserv.ercatec.net/asoka/d/enen/OGM5M2M0Njd8TVJPTi9HTExB/en.1993.1.12.2007.pdf.

[31] SINTAP, Structural Integrity Assessment Procedures for European Industry - Final Procedure, Report No. BE95-1426/FR/7, 1999.

[32] FITNET, FITNET Fitness-for-Service (FFS) – Procedure (Volume I), Revision M, European Thematic Network FITNET, Geesthacht, 2008.

[33] K. Wallin, A Simple Theoretical Charpy V - KIC Correlation for Irradiation Embrittlement. Innovative

Approaches to Irradiation Damage and Fracture Analysis, in: PVP 170, ASME, 1989: pp. 93–100.

[34] P. Nevasmaa, P. Karjalainen-Roikonen, A. Laukkanen, T. Nykänen, A. Ameri, T. Björk, T. Limnell, J. Kuoppala, Fracture characteristics of new ultra- high-strength steel with yield strengths 900 - 960 MPa, in: 2nd Int. Conf. Super-High Strength Steels, Associazione Italiana di Metallurgia, Verona, Italy, 2010.

[35] S. Pallaspuro, T. Limnell, P. Suikkanen, D. Porter, T0 – T28J Correlation of Low-carbon Ultra-high-strength Quenched Steels, Procedia Mater. Sci. 3 (2014) 1032–1037.

[36] K. Wallin, S. Pallaspuro, I. Valkonen, P. Karjalainen-Roikonen, P. Suikkanen, Fracture properties of high performance steels and their welds, Eng. Fract. Mech. 135 (2015) 219–231. doi:10.1016/j.engfracmech.2015.01.007.

[37] S. Pallaspuro, A. Kaijalainen, S. Mehtonen, J. Kömi, Z. Zhang, D. Porter, Effect of microstructure on the impact toughness transition temperature of direct-quenched steels, Mater. Sci. Eng. A. 712 (2018) 671–680. doi:10.1016/j.msea.2017.12.037.

[38] ASTM International, E1921-14a: Standard Test Method for Determination of Reference Temperature, T0, for ferritic Steels in the Transition Range, 2015. doi:10.1520/E1921-05.

[39] ISO, EN ISO 148-1: Metallic Materials, Charpy pendulum impact test, Part 1: Test method, 2009.

[40] ASTM International, E1823-13: Standard Terminology Relating to Fatigue and Fracture Testing, 2013. doi:10.1520/E1823-13.2.

[41] ISO, EN ISO 6892-1: Metallic materials, Tensile testing, Part 1: Method of test at room temperature, 2009.

[42] R. Blondeau, P. Maynier, J. Dollet, B. Vieillard-Baron, Estimation of Hardness, Strength and Elastic Limit of C- and Low-Alloy Steels From Their Composition and Heat Treatment, Mem. Sci. Rev. Met. 72 (1975) 759–769.

[43] J. Trzaska, A. Jagie[33]o, L.A. Dobrzañski, The calculation of CCT diagrams for engineering steels, 2009. http://www.lfs.usp.br/laboratorio/projeto_repositorio/vl01/Estudos/The calculation of CCT diagrams for engineering steels.pdf (accessed November 8, 2018).

[44] M. Pouranvari, S.P.H. Marashi, Critical review of automotive steels spot welding: process, structure and properties, Sci. Technol. Weld. Join. 18 (2013) 361–403. doi:10.1179/1362171813Y.0000000120.

[45] S. Morito, K. Oh-Ishi, K. Hono, T. Ohba, Carbon Enrichment in Retained Austenite Films in Low Carbon Lath Martensite Steel, ISIJ Int. 51 (2011) 1200–1202. https://www.jstage.jst.go.jp/article/isijinternational/51/7/51_7_1200/_pdf (accessed November 8, 2017).

[46] H.-S. Yang, H.K.D.H. Bhadeshia, Austenite grain size and the martensite-start temperature, (2008). doi:10.1016/j.scriptamat.2008.11.043.

[47] A.J. Kaijalainen, P.P. Suikkanen, T.J. Limnell, L.P. Karjalainen, J.I. Kömi, D.A. Porter, Effect of austenite grain structure on the strength and toughness of direct-quenched martensite, J. Alloys Compd. 577 (2013) S642–S648. doi:10.1016/j.jallcom.2012.03.030.

[48] N. Isasti, D. Jorge-Badiola, M.L. Taheri, P. Uranga, Microstructural Features Controlling Mechanical Properties in Nb-Mo Microalloyed Steels. Part II: Impact Toughness, Metall. Mater. Trans. A. 45 (2014) 4972–4982. doi:10.1007/s11661-014-2451-6.

[49] T.L. Anderson, Fracture mechanics: fundamentals and applications, Taylor & Francis, 2005.

[50] J.I. San Martin, J.M. Rodriguez-Ibabe, Determination of energetic parameters controlling cleavage fracture in a

Ti-V microalloyed ferrite-pearlite steel, Scr. Mater. 40 (1999) 459–464. doi:10.1016/S1359-6462(98)00467-9.

[51] J.H. Tweed, J.F. Knott, Micromechanisms of failure in C-Mn weld metals, Acta Metall. 35 (1987) 1401–1414. https://ac.els-cdn.com/0001616087900873/1-s2.0-0001616087900873-main.pdf?_tid=cb30a5e2-cbad-11e7-969c-00000aacb35e&acdnat=1510933476_b46c9e530ac8c24f1d417cf48468a55b (accessed November 17, 2017).